applied sciences

MDPI

Article

Infection Control with Antimicrobial Solid-State ZnO Nanoparticles on Silk Fibroin Gauze

Daniela Vieira [1,†], Cat-Thy Dang [2,†], Rachel Monk [1], Samuel Angel [1], Alexis Marion [2], Uwe Gbureck [3], Edward Harvey [4] and Geraldine Merle [2,*]

[1] Surgical and Interventional Sciences Division, Faculty of Medicine, McGill University, Montreal, QC H3A 2B2, Canada; daniela.vieira@mail.mcgill.ca (D.V.); rachel.monk@mail.mcgill.ca (R.M.); samuel.angel@mail.mcgill.ca (S.A.)
[2] Department of Chemical Engineering, École Polytechnique de Montréal, Montreal, QC H3T 1J4, Canada; cat-thy-aurore.dang@polymtl.ca (C.-T.D.); alexis.marion@umontreal.ca (A.M.)
[3] Department for Functional Materials in Medicine and Dentistry, University of Würzburg, 97070 Würzburg, Germany
[4] Department of Surgery, Faculty of Medicine, McGill University, Montreal, QC H3A 0C5, Canada; edward.harvey@mcgill.ca
* Correspondence: geraldine.merle@polymtl.ca
† These authors contributed equally to this work.

Abstract: Conventional antibiotic treatments for wound infections have the risk of developing microbial resistance, necessitating the search for innovative, alternative solutions like nanoparticles as advanced antibiotics. This work introduces a novel approach for managing acute and chronic wounds by creating an active wound dressing designed to both protect and eliminate bacteria from the injury site. We focused on the electroless deposition of large zinc oxide nanoparticles (ZnO NPs,), aiming for a particle size of around 200 nm to reduce cytotoxicity, onto electrospinned silk fibroin (SF) gauze. We assessed the biocompatibility and antimicrobial effectiveness of the ZnO NP-embedded silk dressing against gram-positive (*Staphylococcus aureus*) and gram-negative (*Pseudomonas aeruginosa*) bacteria. Our analysis indicates that incorporating ZnO nanoparticles into silk wound dressings maintains biocompatibility, achieving 70% cell viability while suppressing the growth of *S. aureus* and *P. aeruginosa*, particularly during the initial 24 h after application. By employing 200 nm particle sizes, we facilitated a significant release of zinc ions without producing harmful reactive oxygen species (ROSs) that could damage both bacteria and host tissues. These findings emphasize the therapeutic potential of bioresorbable bandages enhanced with large ZnO nanoparticles, presenting an innovative approach to clinical wound treatment.

Keywords: electrospinning; electroless deposition; biodegradable; bactericide

check for updates

Citation: Vieira, D.; Dang, C.-T.; Monk, R.; Angel, S.; Marion, A.; Gbureck, U.; Harvey, E.; Merle, G. Infection Control with Antimicrobial Solid-State ZnO Nanoparticles on Silk Fibroin Gauze. *Appl. Sci.* **2024**, *14*, 7103. https://doi.org/10.3390/app14167103

Academic Editor: Junseop Lee

Received: 27 May 2024
Revised: 11 July 2024
Accepted: 5 August 2024
Published: 13 August 2024

Copyright: © 2024 by the authors. Licensee MDPI, Basel, Switzerland. This article is an open access article distributed under the terms and conditions of the Creative Commons Attribution (CC BY) license (https://creativecommons.org/licenses/by/4.0/).

1. Introduction

After the discovery of penicillin in 1928, which provided an effective treatment for bacterial infections, medicine moved towards an era of antibiotics, often referred to as the "golden age" [1]. However, overuse and misuse of antibiotics progressively led to the emergence of antibiotic-resistant bacteria, posing a serious global threat to public health. Bacterial resistance to antibiotics results primarily from genetic mutations altering the target of the drugs or through horizontal gene transfer, enabling the spread of resistance genes. Additionally, bacteria may employ mechanisms by exporting antibiotics outside the bacteria to reduce their action and by producing biofilm to evade antibiotic effects. The misuse of antibiotics accelerates this process, emphasizing the importance of responsible use and ongoing research for combating antibiotic resistance. Alternative strategies include using calcium-dependent antimicrobials [2], chemodynamic therapy [3], and combining several medications [4], leading to increased side effects and greater resistance from bacterial strains

to combinations of antibiotics. The emergence of toxicogenomic tools provides a great asset in understanding and addressing bacterial infections [5]. Through toxicogenomic approaches, the genomic responses of bacteria to antibiotics can be analyzed, gaining insights into resistance mechanisms and potential vulnerabilities. This genomic approach could guide the development of targeted therapies to overcome resistance and enhance the effectiveness of antibacterial treatments. But to pick out the most effective solution to these predictions and uncover new drug targets or more personalized medicine approaches for combating bacterial infections, the genome of the bacteria would require a large number of mutations.

Hospital-associated infections (HAIs) caused by antibiotic-resistant bacteria are a major clinical problem with significant human and economic costs [6,7]. Surgical site infections (SSIs), often caused by skin-dwelling microorganisms, make up 20% of all HAI cases and add up to USD 10 billion annually in U.S. healthcare costs by extending hospital stays [8]. Current treatments for infected wounds, such as negative pressure therapy and surgical debridement, are costly, invasive, and often harmful [9,10]. Topical antibiotics, though widely used, face controversy due to limited evidence of efficacy and rising antibiotic resistance [6,7,10]. However, topical antimicrobial treatments are advantageous because they deliver high concentrations of the active agent directly to the infection site [11]. To address antimicrobial resistance, research has focused on new therapeutic combinations. The selection of appropriate materials for wound dressings is critical for wound healing. An ideal dressing should be biocompatible, non-toxic to skin cells, infection-preventive, and cost-effective [10,12].

Recently, medicated dressings with metal and metal-oxide nanoparticles (NPs) have emerged as alternative antimicrobial agents due to their high biocompatibility and bacterial-killing efficiency [6]. NPs are less likely to develop resistance compared to classical antibiotics because their bactericidal activity targets multiple mechanisms [13,14]. Although the exact mechanisms are not fully understood, the primary lethal factor is thought to be the excessive production of reactive oxygen species (ROSs) on their surface factor [10]. Silver nanoparticles (Ag-NPs) have been widely researched and used in biomedical devices like functionalized fiber dressings and impregnated hydrogels. However, Ag-NPs tend to aggregate, reducing their biofilm penetration effectiveness, and they can be toxic to human cells over long-term use [14,15]. Additionally, the extensive use of Ag-NPs in industries like food and agriculture raises concerns about potential bacterial resistance [16,17]. Zinc oxide (ZnO) nanoparticles are a promising alternative, offering similar bactericidal properties to Ag-NPs. ZnO NPs are highly biocompatible, biodegradable, and have low toxicity in topical applications since they do not penetrate human skin [18–20]. These properties make ZnO NPs an effective antibacterial agent, comparable to Al_2O_3 and SiO_2, and a promising candidate for broadening the use of metal-oxide NPs in biomedical materials [21].

Silk fibroin (SF), derived from natural *Bombyx mori*, offers excellent compatibility with biological tissues, structural integrity, and simplicity of chemical surface alterations. Additionally, SF enhances skin tissue regeneration and healing processes [22,23]. In this research, we seek to improve the antibacterial properties of electrospun silk fibroin gauze by incorporating antimicrobial ZnO nanoparticles through a cost-effective and widely applicable electroless deposition method.

Given that the electroless technique is a chemical reduction process, it allows a controlled and uniform deposition of ZnO nanostructure onto fibrous structures such as electrospun silk fibroin gauze. Electroless deposition does not need an external power source and/or a high temperature for metal deposition, making the process adequate for the medical textile industry. ZnO is chosen for its well-known antimicrobial activity, low toxicity, and biodegradability. The study aims to assess the coated gauze's efficacy in preventing hospital-acquired infections by testing its antimicrobial activity against *S. aureus* and *P. aeruginosa* and quantifying the percentage of bacteria death after 72 h. Additionally, a viability assay with CHO cells is conducted to evaluate cytotoxicity. The ultimate goal of this study is to confirm ZnO as a promising antimicrobial coating for medical textiles that

is bioresorbable and drug-free, contributing to the development of practical solutions for healthcare infection prevention.

2. Materials and Methods

2.1. Preparation of ZnO-SF Gauze

The SF solution was prepared and electrospun following Rockwood et al. [24]. A 6% (*w*/*v*) SF solution was mixed with 5% (*w*/*v*) polyethylene oxide (PEO 900 kDa) to form an SF-PEO aqueous mixture, which was then gently mixed for 10 min at 4 °C. The SF-PEO mixture was loaded into a 1 mL syringe pump equipped with a 27 G needle. SF was electrospun at a 0.6 mL/h flow rate under a 12 kV driving voltage with a 20 cm needle-to-metal-collector distance. The obtained gauzes were soaked in a methanol solution (90% (*v*/*v*)) for 20 min to create insoluble fibers, rinsed in milliQ water for 12 h to eliminate PEO, and then air-dried at room temperature. Electroless deposition was carried out on 1×1 cm^2 pieces of SF gauzes. After immersion in a sensitization aqueous solution of 0.2 M $SnCl_2$ and 0.2 M HCl (Sigma-Aldrich, Oakville, ON, Canada) for 1 h at RT, the gauzes were washed in high-purity water [25]. Next, the SF gauzes were soaked in an activation solution of 0.6 mM $PdCl_2$ (Sigma-Aldrich, Oakville, ON, Canada) and 0.2 M HCl for 30 min at room temperature, followed by careful rinsing with high-purity water. Finally, the gauzes were immersed for 2 h in an aqueous ZnO deposition solution composed of 0.1 M $Zn(NO_3)_2$ and 0.01 M $BH_3NH(CH_3)_2$ (Sigma-Aldrich, Oakville, ON, Canada) at 70 °C, rinsed with milliQ water, and then dried at ambient temperature.

2.2. Physicochemical Characterization

To confirm the electroless ZnO deposition onto silk fibroin gauze, scanning electron microscopy (SEM-Inspect F50-EHT of 2 kV, FEI Company, Hillsboro, OR, USA) was used to study the morphology. The ImageJ software v. 1.54d allowed us to manually analyze the SEM images and measure the size of the ZnO nanoparticles (n = 30) [26]. Energy-dispersive X-ray spectroscopy (EDS-Inspect F50, Oxford Instruments, Abingdon, UK) verified the presence of ZnO nanoparticles. The thermal behavior of the samples was analyzed with thermogravimetric analysis (TGA-Q600 SDT, TA Instruments, New Castle, DE, USA) under a nitrogen atmosphere from 25 °C to 800 °C at 5 °C per min. Fourier transform infrared spectroscopy (FT-IR—PerkinElmer, Waltham, MA, USA) was conducted within a wavenumber range of 4000 to 400 cm^{-1}. The crystalline phase of the ZnO nanoparticles was determined by X-ray diffraction crystallography (XRD-Bruker D8 Discovery Instrument, Bruker Corporation, Milton, ON, Canada), operating at 40 kV and 20 mA with CuKα radiation (λ = 1.5406 Å) and a programmable divergent slit. XRD was recorded in a 2θ range of 20° to 70°. The mechanical properties of 1-cm-long by 1-cm-long gauze samples were assessed by tensile testing (Instron, 3365, Instron, Burlington, ON, Canada) with a 500-N load cell at 10 mm/min.

2.3. In Vitro Assay

Antibacterial properties of ZnO NP gauze against *Pseudomonas aeruginosa* (ATCC® 15442™) and *Staphylococcus aureus* (ATCC® 29213™) were assessed on three samples for each strain. Cultures were carried out overnight in Luria-Bertani (LB) broth media (Thermo Fisher Scientific, Toronto, ON, Canada), then diluted to 1×10^6 CFU/mL with LB broth [27]. Segments measuring 1 cm^2 of ZnO-SF gauze, SF gauze (control), or commercial non-woven surgical gauze (positive control) (Fisherbrand, 22028558, Thermo Fisher Scientific, Toronto, ON, Canada) were incubated in 5 mL of bacterial solution. Live (negative) and dead (positive) controls were utilized to normalize sample data during analysis; both controls consist of a bacterial solution without any sample, with the dead one being processed with ethanol during the assay to kill the bacteria. Samples were maintained in an orbital incubator at 37 °C throughout the experiment until reaching the 24 h, 48 h, or 72 h timepoints. After incubating for 24 h, 48 h, and 72 h, the samples were centrifuged at 10,000× *g* for 10 min and resuspended in 2 mL of Abcam bacterial viability assay kit wash

buffer. A 1 mL suspension from each bacterial sample was then diluted in 5 mL of wash buffer. This process of pelleting, resuspending, and diluting was repeated before staining with the LIVE/DEAD Abcam bacterial viability assay kit (ab189818, Abcam, Shanghai, China). After staining, gauzes were incubated for 1 h in total darkness and then transferred in triplicate to a 96-well plate for fluorescence assessment at 490 nm and 536 nm, and 525 nm and 617 nm, as excitation and emission filters, respectively. The fraction of dead bacteria in each sample was calculated from the readings. We followed the protocol provided with the LIVE/DEAD Abcam Bacterial Viability assay kit (ab189818).

To assess the biocompatibity, Chinese hamster ovary (CHO) cells (ATCC® CLL-61™) were seeded onto ZnO-SF gauze, SF gauze, and commercial non-woven surgical gauze in Dulbecco's Modified Eagle Medium (Gibco, Burlington, ON, Canada) with 10% fetal bovine serum (Gibco, New York, NY, USA), 10 mM HEPES buffer, and 1% penicillin–streptomycin (Gibco) at 37 °C under 5% CO_2. After quantification using Trypan Blue, when they reached 80% confluency, cells containing fewer than 8 passages were plated in a 24-well plate at a density of 1×10^5 cells/mL over sterilized materials. A standard curve from 1×10^3 to 1×10^6 cells/mL and a blank control were prepared. Cell viability was measured using the alamarBlue® Cell Viability Reagent (Invitrogen, 1025) after 24, 28, and 72 h of exposure to 1 cm^2 gauze segments. At each time point, the media was replaced with a fresh solution of complete media with 10% alamarBlue® and incubated for 4 h at 37 °C, protected from light. Following incubation, triplicate samples (n = 3) were transferred to a 96-well plate to measure absorbance at 570 nm and 600 nm. A best-fit line from the OD readings of standards represented cell density. The percent difference in alamarBlue® reduction between exposed and control cells was calculated as per the manufacturer's protocol.

To unravel the antibacterial effect of the ZnO NPs-gauze, ROSs and zinc release were measured. ROSs production was assessed after 24, 48, and 72 h following Vieira et al.'s protocol [7]. Release of all ROSs was evaluated by immersing the 1 cm^2 films into 15 mL vials filled with 4 mL of PBS using a chemically reduced form of fluorescein H2DCFDA as an ROSs indicator. A 25 µM reagent solution of H2DCFDA was produced by dilution with 99.9% ethanol and used as a probe to measure ROS. 200 µL of the sample solution was added into a black microplate (Corning, 3915), and 5 µL of reagent solution was then added and incubated for 10 min wrapped in aluminum foil at room temperature. ROSs release was measured at excitation and emission wavelengths of 488 and 525 nm, respectively. Zinc ion release was performed using a zincon assay adapting Säbel et al.'s protocol [28]. Increasing concentrations of Zn^{2+} solutions were used for zincon assay calibration. After mesh incubation at 37 °C for 24 h, 48 h, and 72 h in PBS solution (1 mL), 25 µL of zincon solution (1.6 mM of zincon in 0.5 M NaOH) was added to 975 µL of the incubation solution and left to react for 5 min at RT to facilitate zincon/zinc complexation. Finally, UV–vis absorbance of the resulting solution was measured in the wavelength range of 300–800 nm (Varioskan LUX spectrophotometer).

2.4. Statistical Methods

Statistical significance for cell viability, bactericidal, and ROSs assays was determined using one-way ANOVA with Tukey's post hoc test. Data analysis was conducted using SPSS software, Version 23.0 (IBM, Armonk, NY, USA), with a significance threshold set at $p < 0.05$. Results are reported as mean ± standard deviation, with all measurements performed in triplicate (n = 3).

3. Results and Discussion

In this work, SF gauze was fabricated via electrospinning, resulting in a uniform distribution and fiber diameter of approximately 500 nm (Figure 1). The incorporation of ZnO nanoparticles visibly increased the roughness of the SF gauze. The electroless deposition method ensured a homogenously high concentration of ZnO nanoparticles with an average diameter of ~230 ± 45 nm on the SF gauze.

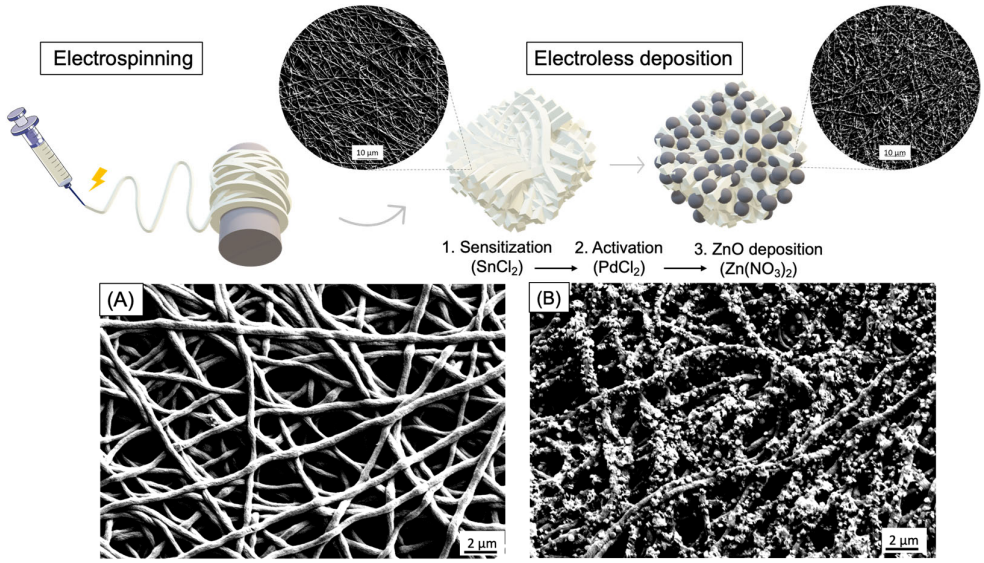

Figure 1. Schematic of electrospinning of SF and ZnO electroless deposition process on SF substrate. SEM images of (**A**) SF gauze and (**B**) ZnO-SF gauze showed a homogeneous distribution of fibers and ZnO nanoparticles.

The deposition of ZnO on various matrices has been already explored; for example, a ZnO was electrodeposited on electrospun polymethylmethacrylate (PMMA) with uniformity and a similar diameter (~200 nm) [25], but polymer has significant drawbacks, such as poor biocompatibility and softness, which hinder its application for bandage [29]. Other combinations, such as ZnO with PLGA/SF [30], were used but, the supporting materials exhibited multiple imperfections and clustered ZnO NPs, potentially affecting the release of active materials. Additionally, the softer surface of the gauze might impact bactericide properties, as a properly roughened surface is known to enhance hydrophobicity and improve antibacterial activity [31]. Electrospun SF was chosen for its ideal softness, making it suitable for wound dressings, while zinc oxide (ZnO) was selected for its antibacterial properties, attributed to the release of Zn ions and its surface roughness. This combination was used as a substrate to grow ZnO nanoparticles (~230 nm) through electroless deposition.

Electroless deposition is usually achieved by immersing the fibers in an aqueous solution containing the metal oxide and a reducing agent; the agent is oxidized, the metal is reduced, and, therefore, deposited on the fibers and attached by electrostatic interactions. This technique was chosen because it does not require the fibers to be conductive; the deposition is harmless to the fibers, uniform, and does not form any aggregate (unlike electrospraying or dipping). It is also simple to achieve as it does not require any current, vacuum system or a high temperature [32]. X-ray diffraction (XRD), Fourier transform infrared spectroscopy (FT-IR), and thermogravimetric analysis (TGA) were carried out to confirm the deposition of ZnO NPs on the SF gauze (Figure 2).

XRD analysis was conducted to assess the crystalline structure of the deposited ZnO nanoparticle (Figure 2A and confirmed with bare ZnO nanoparticles Figure S2A). Both spectra presented peak at 2θ angle of 29°, attributed to the crystalline diffraction of Silk (I) [33]. Other major diffraction peaks at 2θ values of 32.0°, 34.6°, 36.4°, 47.5°, 56.7°, 63.0°, 68.1°, and 69.2° correspond to the hexagonal ZnO diffraction planes, respectively: (100), (002), (101), (102), (110), (103), (112), and (201) in line with the JCPDS (ICDD) card 36-1451 [25,34,35]. It confirms the deposition of a hexagonal wurtzite crystalline ZnO structure with a lattice spacing of a = 0.325 nm and c = 0.521 nm [36]. Wurtzite ZnO crystals are thermodynamic stable structures [37] and offer some antibacterial advantages due to their unique hexagonal structure which enhance Zn^{2+} release and ROSs production, and the sharp edges can physically disrupt bacterial cell walls [38].

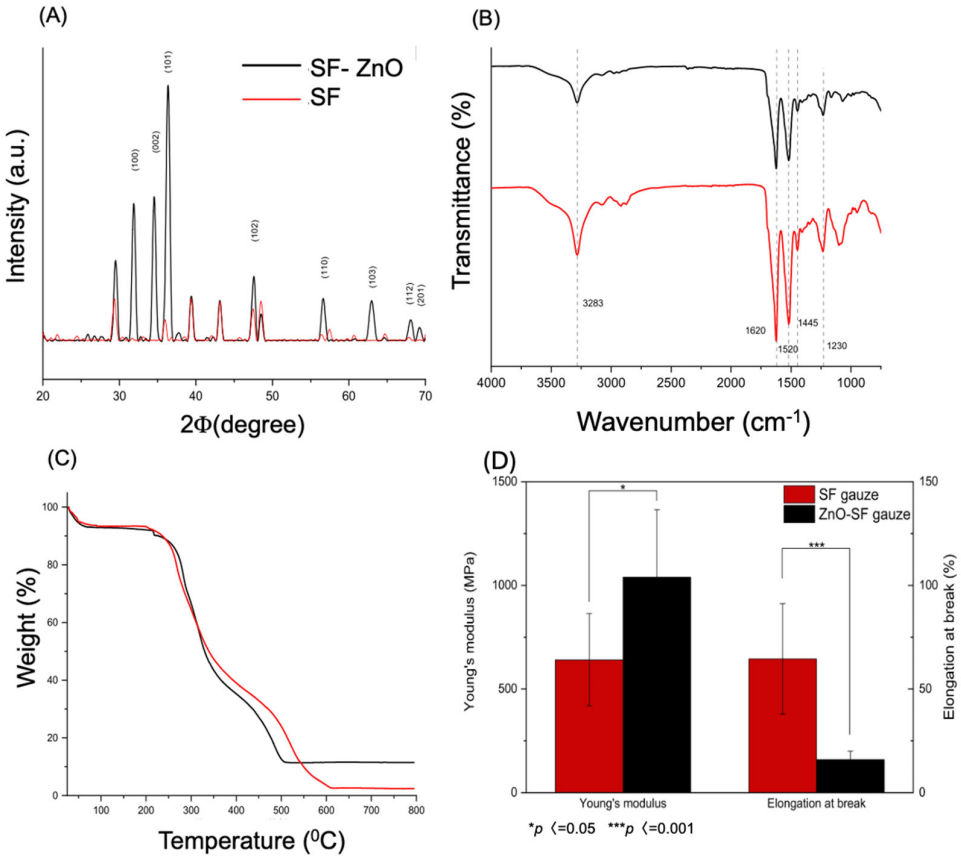

Figure 2. (**A**) XRD patterns, (**B**) FTIR spectra, (**C**) thermal behaviour, and (**D**) Young's modulus and elongation at break of SF and ZnO-SF gauzes, respectively.

The presence of zinc was verified using EDS spectrum analysis (Supplementary Material S1). The chemical composition of SF and ZnO-SF gauzes was determined by FT-IR (Figure 2B). Key SF vibration bands appeared at 1620 cm^{-1}, 1520 cm^{-1}, and 1230 cm^{-1}, corresponding to the primary amides (C=O stretching), secondary amides (N-H bending), and tertiary amides (C-N stretching) of the fibroin protein. The band at 1445 cm^{-1} likely corresponds to asymmetric stretching vibrations of carboxylate groups from amino acids and methyl groups of alanine in SF protein [39]. The shifts in these bands indicate the three-dimensional structure of fibroin proteins, with the band at 1620 cm^{-1} suggesting antiparallel beta-sheet structures characteristic of silk (II) [40,41]. The characteristic SF bands remained unchanged in the ZnO-SF spectra, indicating that the electroless ZnO deposition did not alter the chemical or conformational structure of SF. The attenuation in band intensity was due to ZnO covering parts of the fibers, with a broad band peak at 3506.9 cm^{-1} of bare ZnO nanoparticles attributed to the characteristic absorption of the O-H group (Figure S2B) and a peak at 876 cm^{-1} characteristic of the absorption of the Zn-O bond. The thermal behavior of SF and ZnO-SF gauzes is depicted in Figure 2C. A decrease of approximately 10% in weight, attributed to water loss, is observed from ~25 °C to ~125 °C. Significant mass loss begins around 250 °C, consistent with SF degradation and peptide bond breakdown [7,42]. The mass loss of ZnO-SF gauzes ceases around 500 °C because of the high thermal stability of ZnO (stable even above 800 °C) [43] (Figure S2C: ~3% weight loss for bare ZnO nanoparticles is attributed to the removal of adsorbed water onto the sample). These findings indicate that in this electroless synthesis, ZnO comprises approximately 11.5% of the total weight of the gauzes. The electroless deposition of ZnO-SF gauze led to a modification in the material stiffness with an increase in the Young's modulus from 641 ± 223 MPa to 1040 ± 326 MPa and a decrease in the elongation at the break from 73 ± 18% to 17 ± 4% ($p < 0.001$), yet it is still in the range of skin elongation

(20%) [44] (Figure 2D). No statistically significant modification of the maximal stress was noted (16.5 ± 5.1 MPa and 22.6 ± 3.2 MPa for SF and ZnO-SF gauze, respectively).

The antibacterial properties of materials used for wound dressings are crucial, as they enhance wound healing by minimizing bacterial colonization and infection [45]. The antibacterial efficacy of our materials was evaluated in *S. aureus* and *P. aeruginosa* culture for up to 3 days, in accordance with clinical practices, where wound dressings are typically replaced every 1 to 3 days, depending on the wound type. This timeframe allows for an assessment of the dressing's effectiveness over the typical duration it would be in contact with the wound in a clinical setting [46] (Figure 3A,B).

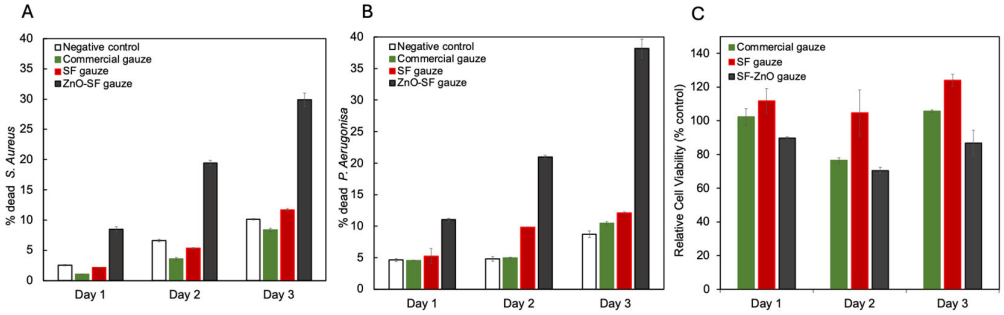

Figure 3. Average percentage of dead (%) (**A**) *S. aureus* and (**B**) *P. aeruginosa* after 24, 48, and 72 h of incubation with various gauzes (n = 3). The color-coded columns represent the four incubation conditions tested: SF, ZnO-SF, and commercial non-woven surgical gauzes. (**C**) Average percentage of relative cell viability (% control) of live CHO cells exposed to various gauzes after 24, 48, and 72 h of incubation (n = 3). The color-coded columns represent the three tested conditions: ZnO-SF, SF, and commercial non-woven surgical gauzes.

In the control groups exposed only to culture media (live), bacterial death was below 10% after 72 h for both strains. For groups treated with SF gauze or commercial non-woven surgical gauze, no significant differences in cell death were noted at any time point. However, the ZnO-SF gauze showed significant antibacterial activity against both bacterial strains, reaching 29.89 ± 1.10% for *S. aureus* and 38.19 ± 1.46% for *P. aeruginosa* after 72 h. The antibacterial effect increased over time, beginning at 8.45 ± 0.44% after 24 h and 19.45 ± 0.42% after 48 h for S. aureus, and 11.03 ± 0.24% after 24 h and 20.97 ± 0.26% after 48 h for *P. aeruginosa*. The ZnO-SF gauze exhibited the highest antibacterial activity, while the SF and commercial surgical gauzes showed minimal to no effect.

The cytotoxicity of ZnO-SF gauze on mammalian cells was assessed using a viability assay conducted on CHO cells exposed to SF, ZnO-SF, and commercial non-woven surgical gauzes for 24, 48, and 72 h (Figure 3C). Normalization was performed on the commercial non-woven surgical gauze, which was assigned 100% viability at each time point. The cell viability did not show any significant differences at 24 and 48 h. Cells exposed to ZnO-SF gauze showed viabilities of 87.75% ± 0.85, 92.17% ± 1.65, and 72.65% ± 7.74 at 24, 48, and 72 h, respectively. Cells exposed to SF gauze had viabilities of 109.34% ± 7.25, 136.82% ± 13.71, and 165.41% ± 3.60 at the same time points. Although there was a statistically significant difference between groups at 72 h, all groups maintained over 70% cell viability throughout the study. ZnO-SF gauze demonstrated 72% cell viability after 72 h, indicating low cytotoxicity (all values > 70%).

On the other hand, a significant difference in bactericidal activity against *S. aureus* and *P. aeruginosa*, two common pathogens responsible for hospital-associated infections, was measured between samples [47]. The ZnO-SF gauze increased bacterial death to over 20% for both strains after 48 h (Figure 3A,B), which is the typical maximum timeline for turnover of surgical dressings [48]. The antimicrobial performance of the ZnO-SF gauze was more pronounced after 72 h of contact with the bacterial culture, with over 25% antibacterial effect, suggesting that ZnO-SF gauze could have a longer useful life than traditional bandages. This can be supported by the fact that lowering the risk of infection

at the wound site is the primary reason for early turnover. This would in turn contribute to lower costs of materials and healthcare labor, as well as lowering the risk of surgical site infection and improving surgical outcomes.

To unravel the mechanism by which the ZnO-SF gauze fights the bacteria, reactive oxygen species (ROSs) generation and Zn^{2+} release were assessed. We did not observe any significant difference in ROSs production between the control, ZnO-SF, and SF gauzes (Figure 4A). However, there was a significant difference in the zinc ion release (p-value < 0.05) when comparing day 1s (0.83 ± 0.10 µg mL^{-1}), 2 (3.98 ± 0.16 µg mL^{-1}), and 3 (5.03 ± 0.12 µg mL^{-1}) (Figure 4B,C). These findings align with the antibacterial effect, showing the highest percentage of dead bacteria after 72 h of exposure (standard curve, Supplementary Materials S2). The Zn^{2+} release ratio from ZnO is lower than those from Zn nanoparticles reported in the literature with sizes <100 nm in the first 100 h where maximum ratios of 80% have been measured [49]. A lower surface area-to-volume ratio provides fewer active zinc atoms on the surface and, consequently, a slower corrosion rate of zinc oxide particles [49]. Bacteria require Zn for growth, with optimal concentrations ranging from 0.0065 µg mL^{-1} to 0.65 µg mL^{-1}. Above 6 µg mL^{-1}, Zn^{2+} becomes cytotoxic to bacterial cells. This occurs because excess Zn^{2+} can compete with other metals for protein binding, leading to improper binding, which in turn causes protein malfunction, inactivation, and denaturation [50]. This cytotoxic effect, as described by Pasquet et al. [51], highlights the potential of ZnO-based wound dressing materials releasing 10 µg mL^{-1} after 72 h to prevent cell death and exhibit antibacterial properties.

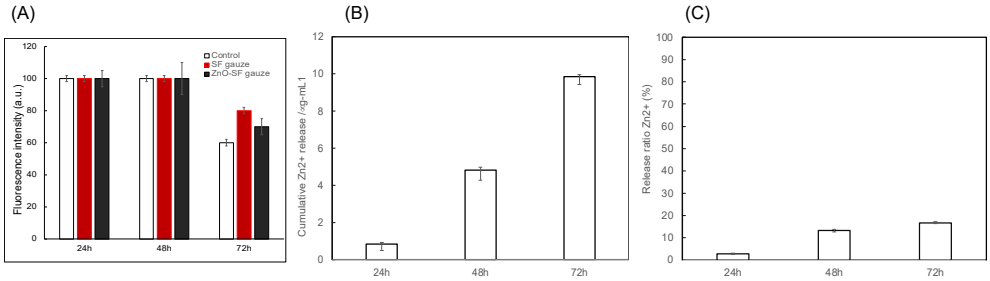

Figure 4. (**A**) Total ROSs production after 24, 48, and 72 h of incubation in PBS (C, control), SF gauze (SF), and ZnO-SF gauze (ZnO). (**B**) Zn^{2+} release for ZnO-SF gauze after 24 h, 48 h, and 72 h (n = 3, p-value < 0.05, significant difference between time points) and (**C**) Zn^{2+} release ratio from zinc particles. The release ratio is the amount of zinc ions released to the total amount of zinc on the SF gauze.

While the exact toxicity mechanism of ZnO towards bacteria is still controversial, the potential antibacterial effects can be attributed to the following three main mechanisms [52]: (1) ROSs production resulting in the disintegration of the bacterial membrane; (2) Zn^{2+} release disrupting critical processes including DNA replication and protein synthesis [53]; and (3) direct interaction between ZnO NPs and bacteria causing antimicrobial effects [54,55]. A significant factor in the antibacterial properties of ZnO is ROSs production, i.e., hydroxyl radicals, H_2O_2, and singlet oxygen [56]. Although the precise mechanism remains unclear, nanoparticle size-dependent ROSs production appears to impact bacterial death. Indeed, smaller particles exhibit a greater surface area, which facilitates interactions with cellular constituents and elevated ROSs generation. Additionally, smaller particles can show increased reactivity because of their elevated surface energy, leading to greater ROSs production. In this work, the results demonstrated insufficient ROS production, probably caused by the large ZnO nanoparticle size. Indeed, several studies (Table 1) have studied the antibacterial properties of ZnO NP (<100 nm) on different substrates [21,57–60]. ZnO NP with sizes <100 nm is known to exhibit better antibacterial properties than larger sizes [59].

Table 1. Comparative antibacterial effect of different biodegradable ZnO-coated mat.

Material	Size	Concentration	Gram + Antimicrobial Activity	Gram − Antimicrobial Activity	Cell Viability
SF/ZnO	230 ± 45 nm	11.5% wt	29.89 ± 1.10% (Live/dead assay, 72 h, *S. aureus*)	38.19 ± 1.46% (Live/dead assay, 72 h, *P. aeruginosa*)	>80, 90, 70% after 24, 48 and 72 h (Alamar Blue Assay, CHO)
PLGA/SF/ZnO [22]	30–40 nm	1%, 2%, 3% (*v*/*v*)	45.1%, 87.57%, 100% (turbidity, *S. aureus*) Found MIC = 39.06 µg/mL (turbidity, 24 h, *S. aureus*)	30.54%, 75.42%, 98.63% (turbidity, *E. coli*) Found MIC = 78.12 µg/mL (turbidity, 24 h, *E. coli*)	Same as PLGA/SF for day 1, 3, 7; cytotoxic at day 3 and 7; cytotoxic at day 3 and 7 (CCK8 Assay, L929)
PVA/CS/ZnO [40]	30 nm	0.5%, 1% wt	75%, 85% (OD, 24 h, *S. aureus*)	70%, 80% (OD, 24 h, *E. coli*)	74%, >85% (24 h) >80%, >80% (48 h) (MTT assay, L929)
Electrospun PVA/ZnO [41]	50–150 nm	500 µg/mL	MIC = 250 µg/mL MBC = 250 µg/mL (24 h, *S. aureus*)	MIC = 62.5 µg/mL MBC = 125 µg/mL (24 h, *E. coli*)	82.8%, 48 h (MTT assay, HFF)
PVA/starch/ZnO [42]	<100 nm	2.6%, 3.2%, 3.8%, 4.4% wt	Significant (agar diffusion assay, 48 h, *S. aureus*)	Significant (agar diffusion assay, 48 h, *E. coli*)	N/A
CS/ZnO [43]	80 nm	0.001%, 0.0025%, 0.005%, 0.01%	Significant for all but 0.001% (still decreased number of bacteria) Best with higher concentrations of ZnO NP (colony counting, 24 h, *S. aureus*)	Significant for all (colony counting, 24 h, *E. coli*)	0.01%: >80% viability after 24, 48 and 72 h Others: toxicity after 24 h (<60%) but good viability afterwards (>80%) (cell staining, nHDF)
Co-electrospun HA/SF-ZnO [33]	<50 nm	6.5%, 19.35%, 32.26% wt (A VERIFIER)	116 ± 3, 42 ± 2, and 6 ± 1 bacteria (CFU, 24 h, *S. aureus*) Antibacterial effect increases with concentration	267 ± 7, 79 ± 3, and 28 ± 2 bacteria (CFU, 24 h, *E. coli*) Antibacterial effect increases with concentration	> 85% for all, but 32.26% wt decreased with time (1, 3, 7 days, MTT assay, HaCat)
PLA/ZnO [45]	48 nm	0.5, 1, 2%	86%, 93%, 98% (colony counting, 72 h, *S. aureus*)	40%, 57%, 75% (colony counting, 72 h, *E. coli*)	79.6% (ZnO 2%wt, MTT Assay, 72 h, HSF) 70.5% (ZnO 2%wt, MTT Assay, 72 h, MSC)
PDLA/ZnO [46]	6.36 ± 2.08 nm	1, 3, 5% wt	69.07 ± 1.07%, 69.01 ± 36.92%, 97.07 ± 2.63% (24 h, *S. aureus*)	8.12 ± 2.49%, 25.50 ± 12.20%, 99.59 ± 0.14% (24 h, *E. coli*)	For all samples: 80% day 1 and 3, >100% day 5 and 7 (resazurin, MC3T3-E1)
PLA/PCL/TPS (thermoplastic starch)/ZnO [47]	30–50 nm	3%, 5% wt	10 mm, 12 mm (inhibition zone, 24 h, *S. aureus*)	8 mm, 9 mm (inhibition zone, 24 h, *E. coli*)	25%, 15%: cytotoxic (MTT assay, 24 h, L929)

This size-dependent toxicity is further accentuated by the increased internalization of smaller particles within bacteria, thereby enhancing their antibacterial efficiency compared to larger particles at the same concentration [53]. Based on the obtained results, the larger size of the ZnO nanoparticles causing lower internalization, and weak ROSs production, it can be inferred that the significant release of Zn^{2+} ions in the medium is the logical cause of ZnO toxicity toward *S. aureus* and *P. aeruginosa*. The main proposed antibacterial mechanism for Zn^{2+} uptake is linked to active transport inhibition, amino acid metabolism, and enzyme system disruption [38]. However, these aspects, i.e., ROSs, Zn, and internalization, also apply to cells, thereby causing great cytotoxicity [53]. The gain of antibacterial activity is, however, negatively correlated with biosafety and cell viability [61,62]. Consequently, a greater particle size (with a smaller specific surface area) was chosen to minimize the cytotoxicity of ZnO particles. This approach slows down the dissolution kinetics of the ZnO particles and reduces the number of particles internalized by cells, resulting in decreased cytotoxic effects [63]. Indeed, with FDA approval for the use of ZnO in bulk and with a size exceeding 100 nm [64], our material (230 ± 45 nm) is considered safe. The size of nanoparticles (NPs) plays a key role in dictating their unique interactions with cells. It was demonstrated that smaller ZnO nanoparticles (30 nm) had a higher internalization effect compared to larger nanoparticles

(80–100 nm) and the ionic form of zinc [65]. NP sizes ranging from 1 to 100 nm align with the dimensions of protein globules, DNA helixes, and cell membranes, facilitating easy entry into cells and organelles. Studies, such as those by Huo et al. and Pan et al., highlight that smaller NPs, around 6 nm or less, can penetrate the cell nucleus, while larger ones (10 or 16 nm) remain in the cytoplasm, revealing a size-dependent toxicity [66]. Below 2 nm, NPs induce apoptosis and cell necrosis [67]. Furthermore, NP size influences interactions with cell transport and defense systems, affecting distribution kinetics. NPs smaller than 5 nm tend to overcome cell barriers non-specifically, while larger particles enter cells through various mechanisms such as pinocytosis [68]. It was demonstrated that smaller ZnO nanoparticles (30 nm) had a higher internalization effect compared to larger nanoparticles (80–100 nm) and the ionic form of zinc [65]. To improve the bactericidal effect of the gauze without modifying the cytotoxicity, more research should be performed to increase the release of Zn^{2+} and maintain the low rate of ROSs formation. For example, strategies include surface modification with acidic coatings to promote dissolution, reduce particle agglomeration, or increasing the porosity of the gauze to allow better fluid penetration. In vivo experiments indicate rapid distribution of NPs smaller than 10 nm among all organs and tissues, contrasting with the localization of larger NPs (around 250 nm) in specific organs (liver and spleen) [69]. Our material, coated with ZnO nanoparticles larger than 100 nm, not only induces bacterial death but also preserves tissues and could support essential physiological processes involved in tissue repair. The low release of ROSs from our dressing enhances tissue safety, making it particularly suitable for clinical treatment of chronic diabetic wounds, aiming to improve wound healing and prevent bacterial infections [70,71]. The results of these in vitro studies lay the groundwork for further research in vivo, guiding the development of wound dressings that effectively combat bacterial growth and facilitate the healing process [72]. Given that silk-based materials have been approved by the FDA for a wide array of applications, such as wound dressing, and ZnO is FDA-approved for skin-protection and wound-care products, some of the regulatory considerations have already been addressed, but for full implementation in clinical settings, safety assessments, manufacturing scalability, and clinical efficacy studies will be required.

4. Conclusions

A novel electrospun silk fibroin gauze was coated with antimicrobial zinc oxide nanoparticles using an efficient and scalable electroless deposition method. This innovative material shows significant potential for reducing hospital-acquired infections. ZnO was chosen for its antimicrobial properties, low toxicity, and biodegradability, making it a superior choice among metal oxides. The gauze's antimicrobial efficacy was tested, showing a 29.9% $\pm$ 1.1% reduction in *S. aureus* bacteria and a 38.2% $\pm$ 1.5% reduction in *P. aeruginosa* bacteria after 72 h. Cytotoxicity was evaluated using a viability assay with CHO cells, revealing over 70% cell viability across all conditions and exposure times. This study highlights the promise of ZnO-coated silk fibroin gauze as an antimicrobial agent in medical textiles and suggests further optimization of Zn^{2+} loading to enhance its effectiveness in preventing healthcare-associated infections. Future studies should focus on these optimizations and include biofilm assessment to address the more challenging aspects of biofilm-related infections. This comprehensive approach will better inform the development of advanced wound care solutions.

Supplementary Materials: The following supporting information can be downloaded at: https://www.mdpi.com/article/10.3390/app14167103/s1. Figure S1. EDS spectrum of ZnO-SF silk fibroin gauze. Figure S2. (A) XRD patterns, (B) FTIR spectra, (C) Thermal behaviour of ZnO nanoparticles. Figure S3. Standard curve for zinc ions release measurement.

Author Contributions: Conceptualization, D.V. and G.M.; methodology, D.V., R.M. and S.A.; validation, D.V., R.M. and S.A.; formal analysis, D.V., R.M. and S.A.; resources, G.M.; data curation, D.V., R.M. and S.A.; writing—original draft preparation, D.V., C.-T.D. and A.M.; writing—review and editing, E.H., U.G. and G.M.; supervision, G.M.; funding acquisition, G.M. and U.G. All authors have read and agreed to the published version of the manuscript.

Funding: This research was funded by Merle, NSERC: RGPIN-2020-05884; FRQS chercheur boursier: 266388.

Data Availability Statement: Data is contained within the article or Supplementary Materials. The data presented in this study are available on request from the corresponding author.

Conflicts of Interest: There are no conflicts to declare.

References

1. Gaynes, R. The Discovery of Penicillin—New Insights After More Than 75 Years of Clinical Use. *Emerg. Infect. Dis.* **2017**, *23*, 849–853. [CrossRef]
2. Wang, Z.; Zeng, Y.; Ahmed, Z.; Qin, H.; Bhatti, I.A.; Cao, H. Calcium-dependent antimicrobials: Nature-inspired materials and designs. *Exploration* **2024**, 20230099. [CrossRef]
3. Zhang, J.; Guo, H.; Liu, M.; Tang, K.; Li, S.; Fang, Q.; Du, H.; Zhou, X.; Lin, X.; Yang, Y.; et al. Recent design strategies for boosting chemodynamic therapy of bacterial infections. *Exploration* **2024**, *4*, 20230087. [CrossRef] [PubMed]
4. Huang, F.; Cai, X.; Hou, X.; Zhang, Y.; Liu, J.; Yang, L.; Liu, Y.; Liu, J. A dynamic covalent polymeric antimicrobial for conquering drug-resistant bacterial infection. *Exploration* **2022**, *2*, 20210145. [CrossRef]
5. Singh, A.V.; Chandrasekar, V.; Paudel, N.; Laux, P.; Luch, A.; Gemmati, D.; Tisato, V.; Prabhu, K.S.; Uddin, S.; Dakua, S.P. Integrative toxicogenomics: Advancing precision medicine and toxicology through artificial intelligence and OMICs technology. *Biomed. Pharmacother.* **2023**, *163*, 114784. [CrossRef] [PubMed]
6. Vieira, D.; Angel, S.N.; Honjol, Y.; Masse, M.; Gruenheid, S.; Harvey, E.J.; Merle, G. Engineering surgical stitches to prevent bacterial infection. *Sci. Rep.* **2022**, *12*, 834. [CrossRef] [PubMed]
7. Vieira, D.; Angel, S.; Honjol, Y.; Gruenheid, S.; Gbureck, U.; Harvey, E.; Merle, G. Electroceutical Silk–Silver Gel to Eradicate Bacterial Infection. *Adv. Biosyst.* **2020**, *4*, 1900242. [CrossRef] [PubMed]
8. Ban, K.A.; Minei, J.P.; Laronga, C.; Harbrecht, B.G.; Jensen, E.H.; Fry, D.E.; Itani, K.M.; E Dellinger, P.; Ko, C.Y.; Duane, T.M. American College of Surgeons and Surgical Infection Society: Surgical site infection guidelines, 2016 update. *J. Am. Coll. Surg.* **2017**, *224*, 59–74. [CrossRef] [PubMed]
9. Anghel, E.L.; DeFazio, M.V.; Barker, J.C.; Janis, J.E.; Attinger, C.E. Current concepts in debridement: Science and strategies. *Plast. Reconstr. Surg.* **2016**, *138*, 82S–93S. [CrossRef]
10. Han, G.; Ceilley, R. Chronic wound healing: A review of current management and treatments. *Adv. Ther.* **2017**, *34*, 599–610. [CrossRef]
11. Williamson, D.A.; Carter, G.P.; Howden, B.P. Current and emerging topical antibacterials and antiseptics: Agents, action, and resistance patterns. *Clin. Microbiol. Rev.* **2017**, *30*, 827–860. [CrossRef] [PubMed]
12. Negut, I.; Grumezescu, V.; Grumezescu, A.M. Treatment strategies for infected wounds. *Molecules* **2018**, *23*, 2392. [CrossRef] [PubMed]
13. Lee, N.Y.; Ko, W.C.; Hsueh, P.R. Nanoparticles in the treatment of infections caused by multidrug-resistant organisms. *Front. Pharmacol.* **2019**, *10*, 1153. [CrossRef]
14. Xu, C.; Akakuru, O.U.; Ma, X.; Zheng, J.; Zheng, J.; Wu, A. Nanoparticle-based wound dressing: Recent progress in the detection and therapy of bacterial infections. *Bioconjug. Chem.* **2020**, *31*, 1708–1723. [CrossRef]
15. Kalantari, K.; Mostafavi, E.; Afifi, A.M.; Izadiyan, Z.; Jahangirian, H.; Rafiee-Moghaddam, R.; Webster, T.J. Wound dressings functionalized with silver nanoparticles: Promises and pitfalls. *Nanoscale* **2020**, *12*, 2268–2291. [CrossRef] [PubMed]
16. Graves Jr, J.L.; Tajkarimi, M.; Cunningham, Q.; Campbell, A.; Nonga, H.; Harrison, S.H.; Barrick, J.E. Rapid evolution of silver nanoparticle resistance in Escherichia coli. *Front. Genet.* **2015**, *6*, 42. [CrossRef] [PubMed]
17. Panáček, A.; Kvítek, L.; Smékalová, M.; Večeřová, R.; Kolář, M.; Röderová, M.; Dyčka, F.; Šebela, M.; Prucek, R.; Tomanec, O.; et al. Bacterial resistance to silver nanoparticles and how to overcome it. *Nat. Nanotechnol.* **2018**, *13*, 65–71. [CrossRef]
18. Rosenberg, M.; Visnapuu, M.; Vija, H.; Kisand, V.; Kasemets, K.; Kahru, A.; Ivask, A. Selective antibiofilm properties and biocompatibility of nano-ZnO and nano-ZnO/Ag coated surfaces. *Sci. Rep.* **2020**, *10*, 13478. [CrossRef]
19. Zhang, Y.; Nayak, T.; Hong, H.; Cai, W. Biomedical applications of zinc oxide nanomaterials. *Curr. Mol. Med.* **2013**, *13*, 1633–1645. [CrossRef]
20. Jiang, J.; Pi, J.; Cai, J. The advancing of zinc oxide nanoparticles for biomedical applications. *Bioinorg. Chem. Appl.* **2018**, *2018*, 1062562. [CrossRef]
21. Jiang, W.; Mashayekhi, H.; Xing, B. Bacterial toxicity comparison between nano- and micro-scaled oxide particles. *Environ. Pollut.* **2009**, *157*, 1619–1625. [CrossRef] [PubMed]
22. Pollini, M.; Paladini, F. Bioinspired materials for wound healing application: The potential of silk fibroin. *Materials* **2020**, *13*, 3361. [CrossRef] [PubMed]
23. Zhang, W.; Chen, L.; Chen, J.; Wang, L.; Gui, X.; Ran, J.; Xu, G.; Zhao, H.; Zeng, M.; Ji, J.; et al. Silk fibroin biomaterial shows safe and effective wound healing in animal models and a randomized controlled clinical trial. *Adv. Healthc. Mater.* **2017**, *6*, 1700121. [CrossRef] [PubMed]
24. Rockwood, D.N.; Preda, R.C.; Yücel, T.; Wang, X.; Lovett, M.L.; Kaplan, D.L. Materials fabrication from Bombyx mori silk fibroin. *Nat. Protoc.* **2011**, *6*, 1612–1631. [CrossRef] [PubMed]

25. Preda, N.; Evanghelidis, A.; Enculescu, M.; Florica, C.; Enculescu, I. Zinc oxide electroless deposition on electrospun PMMA fiber mats. *Mater. Lett.* **2015**, *138*, 238–242. [CrossRef]
26. Singh, A.V.; Bansod, G.; Mahajan, M.; Dietrich, P.; Singh, S.P.; Rav, K.; Thissen, A.; Bharde, A.M.; Rothenstein, D.; Kulkarni, S.; et al. Digital Transformation in Toxicology: Improving Communication and Efficiency in Risk Assessment. *ACS Omega* **2023**, *8*, 21377–21390. [CrossRef] [PubMed]
27. Joshi, K.M.; Shelar, A.; Kasabe, U.; Nikam, L.K.; Pawar, R.A.; Sangshetti, J.; Kale, B.B.; Singh, A.V.; Patil, R.; Chaskar, M.G. Biofilm inhibition in Candida albicans with biogenic hierarchical zinc-oxide nanoparticles. *Biomater. Adv.* **2022**, *134*, 112592. [CrossRef] [PubMed]
28. Säbel, C.E.; Neureuther, J.M.; Siemann, S. A spectrophotometric method for the determination of zinc, copper, and cobalt ions in metalloproteins using Zincon. *Anal. Biochem.* **2010**, *397*, 218–226. [CrossRef] [PubMed]
29. Chae, M.J.; Kim, D.W.; Kim, Y.J.; Kweon, H.Y.; Cho, Y.-J.; Choi, S.Y.; Lee, H.R. Toxicity assessment of a novel silk fibroin and poly-methyl-methacrylate composite material. *Mol. Cell. Toxicol.* **2014**, *10*, 277–283. [CrossRef]
30. Huang, K.; Jinzhong, Z.; Zhu, T.; Morsi, Y.; Aldalbahi, A.; El-Newehy, M.; Yan, X.; Mo, X. Exploration of the antibacterial and wound healing potential of a PLGA/silk fibroin based electrosp. *J. Mater. Chem. B.* **2021**, *9*, 1452–1465.
31. Seyfi, J.; Goodarzi, V.; Wurm, F.R.; Shojaei, S.; Jafari-Nodoushan, M.; Najmoddin, N.; Khonakdar, H.A.; Baghersad, M.H.; Uzun, L. Developing antibacterial superhydrophobic coatings based on polydimethylsiloxane/silver phosphate nanocomposites: Assessment of surface morphology, roughness and chemistry. *Prog. Org. Coat.* **2020**, *149*, 105944. [CrossRef]
32. Pinto, N.; Silva, A.N.; Rosim-Fachini, E.; Carrión, P.; Furlan, R.; Ramos, I. Electroless deposition of thin metallic films on polymer fibers prepared via electrospinning. *Polym. Prepr.* **2003**, *44*, 138–139.
33. Lu, Q.; Hu, X.; Wang, X.; Kluge, J.A.; Lu, S.; Cebe, P.; Kaplan, D.L. Water-insoluble silk films with silk I structure. *Acta Biomater.* **2010**, *6*, 1380–1387. [CrossRef] [PubMed]
34. Dinesh, V.P.; Biji, P.; Ashok, A.; Dhara, S.K.; Kamruddin, M.; Tyagi, A.K.; Raj, B. Plasmon-mediated, highly enhanced photocatalytic degradation of industrial textile dyes using hybrid ZnO@Ag core–shell nanorods. *RSC Adv.* **2014**, *4*, 58930–58940. [CrossRef]
35. Xu, J.; Su, H.; Han, J.; Chen, Y.; Song, W.; Gu, Y.; Moon, W.-J.; Zhang, D. In situ deposition of flower-like ZnO on silk fibroin fibers. *Appl. Phys. A* **2012**, *108*, 235–238. [CrossRef]
36. Guo, L.; Ji, Y.L.; Xu, H.; Simon, P.; Wu, Z. Regularly shaped, single-crystalline ZnO nanorods with wurtzite structure. *J. Am. Chem. Soc.* **2002**, *124*, 14864–14865. [CrossRef] [PubMed]
37. Li, T.; Cai, H.; Li, C.; Liu, X.; Huang, F. Rocksalt-Zincblende-Wurtzite Mixed-Phase ZnO Crystals With High Activity as Photocatalysts for Visible-Light-Driven Water Splitting. *Front. Chem.* **2020**, *8*, 351. [CrossRef]
38. Sirelkhatim, A.; Mahmud, S.; Seeni, A.; Kaus, N.H.M.; Ann, L.C.; Bakhori, S.K.M.; Hasan, H.; Mohamad, D. Review on Zinc Oxide Nanoparticles: Antibacterial Activity and Toxicity Mechanism. *Nanomicro Lett.* **2015**, *7*, 219–242. [CrossRef]
39. Zhang, H.; Li, L.; Dai, F.; Zhang, H.-H.; Ni, B.; Zhou, W.; Yang, X.; Wu, Y.-Z. Preparation and characterization of silk fibroin as a biomaterial with potential for drug delivery. *J. Transl. Med.* **2012**, *10*, 117. [CrossRef]
40. Boulet-Audet, M.; Vollrath, F.; Holland, C. Identification and classification of silks using infrared spectroscopy. *J. Exp. Biol.* **2015**, *218*, 3138–3149. [CrossRef]
41. Ha, S.W.; Tonelli, A.E.; Hudson, S.M. Structural studies of bombyx mori silk fibroin during regeneration from solutions and wet fiber spinning. *Biomacromolecules* **2005**, *6*, 1722–1731. [CrossRef] [PubMed]
42. Motta, A.; Fambri, L.; Migliaresi, C. Regenerated silk fibroin films: Thermal and dynamic mechanical analysis. *Macromol. Chem. Phys.* **2002**, *203*, 1658–1665. [CrossRef]
43. Jones, F.; Tran, H.; Lindberg, D.; Zhao, L.; Hupa, M. Thermal stability of zinc compounds. *Energy Fuels* **2013**, *27*, 5663–5669. [CrossRef]
44. Kalra, A.; Lowe, A.; Al-Jumaily, A.M. Mechanical Behaviour of Skin: A Review. *J. Mater. Sci. Eng.* **2016**, *5*, 1000254.
45. Hadisi, Z.; Farokhi, M.; Bakhsheshi-Rad, H.R.; Jahanshahi, M.; Hasanpour, S.; Pagan, E.; Dolatshahi-Pirouz, A.; Zhang, Y.S.; Kundu, S.C.; Akbari, M. Hyaluronic Acid (HA)-Based Silk Fibroin/Zinc Oxide Core-Shell Electrospun Dressing for Burn Wound Management. *Macromol. Biosci.* **2020**, *20*, e1900328. [CrossRef] [PubMed]
46. Britto, E.J.; Nezwek, T.A.; Popowicz, P.; Robins, M. *Wound Dressings*; StatPearls, Ed.; StatPearls Publishing: Treasure Island, FL, USA, 2024.
47. Slayton, R.B.; Toth, D.; Lee, B.Y.; Tanner, W.; Bartsch, S.M.; Khader, K.; Wong, K.; Brown, K.; McKinnell, J.A.; Ray, W.; et al. Vital signs: Estimated effects of a coordinated approach for action to reduce antibiotic-resistant infections in health care facilities—United States. *MMWR Morb. Mortal. Wkly. Rep.* **2015**, *64*, 826. [CrossRef] [PubMed]
48. Toon, C.D.; Ramamoorthy, R.; Davidson, B.R.; Gurusamy, K.S. Early versus delayed dressing removal after primary closure of clean and clean-contaminated surgical wounds. *Cochrane Database Syst. Rev.* **2015**, *2015*, CD010259. [CrossRef] [PubMed]
49. Yang, Z.; Xie, C. Zn^{2+} release from zinc and zinc oxide particles in simulated uterine solution. *Colloids Surf. B Biointerfaces* **2006**, *47*, 140–145. [CrossRef] [PubMed]
50. Godoy-Gallardo, M.; Eckhard, U.; Delgado, L.M.; de Roo Puente, Y.J.D.; Hoyos-Nogués, M.; Gil, F.J.; Perez, R.A. Antibacterial approaches in tissue engineering using metal ions and nanoparticles: From mechanisms to applications. *Bioact. Mater.* **2021**, *6*, 4470–4490. [CrossRef]
51. Pasquet, J.; Chevalier, Y.; Pelletier, J.; Couval, E.; Bouvier, D.; Bolzinger, M.-A. The contribution of zinc ions to the antimicrobial activity of zinc oxide. *Colloids Surf. A: Physicochem. Eng. Asp.* **2014**, *457*, 263–274. [CrossRef]

52. Azam, A.; Ahmed, A.S.; Oves, M.; Khan, M.S.; Habib, S.S.; Memic, A. Antimicrobial activity of metal oxide nanoparticles against Gram-positive and Gram-negative bacteria: A comparative study. *Int. J. Nanomed.* **2012**, *7*, 6003–6009. [CrossRef] [PubMed]
53. Chong, W.J.; Shen, S.; Li, Y.; Trinchi, A.; Simunec, D.P.; Kyratzis, I.L.; Sola, A.; Wen, C. Biodegradable PLA-ZnO nanocomposite biomaterials with antibacterial properties, tissue engineering viability, and enhanced biocompatibility. *Smart Mater. Manuf.* **2022**, *1*, 100004. [CrossRef]
54. Zhan, J.; Zhang, W.; Wang, M.; Guan, W.; Yan, X.; Zhang, Q.; Wang, H.; Wang, Z.; Zhang, Y.; Zou, L. Fabrication, characterization and antibacterial properties of ZnO nanoparticles decorated electrospun polyacrylonitrile nanofibers membranes. *Mater. Today Commun.* **2022**, *32*, 103958. [CrossRef]
55. Shankar, S.; Wang, L.F.; Rhim, J.W. Incorporation of zinc oxide nanoparticles improved the mechanical, water vapor barrier, UV-light barrier, and antibacterial properties of PLA-based nanocomposite films. *Mater. Sci. Eng. C Mater. Biol. Appl.* **2018**, *93*, 289–298. [CrossRef] [PubMed]
56. Dobrucka, R.; Dlugaszewska, J.; Kaczmarek, M. Cytotoxic and antimicrobial effects of biosynthesized ZnO nanoparticles using of Chelidonium majus extract. *Biomed. Microdevices* **2018**, *20*, 5. [CrossRef] [PubMed]
57. Vandebriel, R.J.; De Jong, W.H. A review of mammalian toxicity of ZnO nanoparticles. *Nanotechnol. Sci. Appl.* **2012**, *5*, 61–71. [CrossRef] [PubMed]
58. Liu, J.; Kang, Y.; Yin, S.; Song, B.; Wei, L.; Chen, L.; Shao, L. Zinc oxide nanoparticles induce toxic responses in human neuroblastoma SHSY5Y cells in a size-dependent manner. *Int. J. Nanomed.* **2017**, *12*, 8085–8099. [CrossRef] [PubMed]
59. Jin, M.; Li, N.; Sheng, W.; Ji, X.; Liang, X.; Kong, B.; Yin, P.; Li, Y.; Zhang, X.; Liu, K. Toxicity of different zinc oxide nanomaterials and dose-dependent onset and development of Parkinson's disease-like symptoms induced by zinc oxide nanorods. *Environ. Int.* **2021**, *146*, 106179. [CrossRef] [PubMed]
60. Hanley, C.; Thurber, A.; Hanna, C.; Punnoose, A.; Zhang, J.; Wingett, D.G. The Influences of Cell Type and ZnO Nanoparticle Size on Immune Cell Cytotoxicity and Cytokine Induction. *Nanoscale Res. Lett.* **2009**, *4*, 1409–1420. [CrossRef]
61. Orazizadeh, M.; Khodadadi, A.; Bayati, V.; Saremy, S.; Farasat, M.; Khorsandi, L. In Vitro Toxic Effects of Zinc Oxide Nanoparticles on Rat Adipose Tissue-Derived Mesenchymal Stem Cells. *Cell J.* **2015**, *17*, 412–421. [CrossRef]
62. Chen, F.-C.; Huang, C.-M.; Yu, X.-W.; Chen, Y.-Y. Effect of nano zinc oxide on proliferation and toxicity of human gingival cells. *Human. Exp. Toxicol.* **2022**, *41*, 09603271221080236. [CrossRef]
63. Badry, A.; Ibrahim, A.A.E.H.; Said, M.I.; Nasr, A.A.E.; Mohamed, M.A.; Hassan, A.K.; Safwat, M.M. In vitro assessment of PEG-6000 coated-ZnO nanoparticles: Modulating action to the resisted antibiotic activity against APEC. *BMC Vet. Res.* **2023**, *19*, 1. [CrossRef]
64. Chong, S.F.; Smith, A.A.; Zelikin, A.N. Microstructured, functional PVA hydrogels through bioconjugation with oligopeptides under physiological conditions. *Small* **2013**, *9*, 942–950. [CrossRef] [PubMed]
65. Lopes, S.; Ribeiro, F.; Wojnarowicz, J.; Łojkowski, W.; Jurkschat, K.; Crossley, A.; Soares, A.M.; Loureiro, S. Zinc oxide nanoparticles toxicity to Daphnia magna: Size-dependent effects and dissolution. *Environ. Toxicol. Chem.* **2014**, *33*, 190–198. [CrossRef] [PubMed]
66. Huo, S.; Jin, S.; Ma, X.; Xue, X.; Yang, K.; Kumar, A.; Wang, P.C.; Zhang, J.; Hu, Z.; Liang, X.-J. Ultrasmall Gold Nanoparticles as Carriers for Nucleus-Based Gene Therapy Due to Size-Dependent Nuclear Entry. *ACS Nano* **2014**, *8*, 5852–5862. [CrossRef] [PubMed]
67. Pan, Y.; Neuss, S.; Leifert, A.; Fischler, M.; Wen, F.; Simon, U.; Schmid, G.; Brandau, W.; Jahnen-Dechent, W. Size-Dependent Cytotoxicity of Gold Nanoparticles. *Small* **2007**, *3*, 1941–1949. [CrossRef] [PubMed]
68. Zhang, S.; Gao, H.; Bao, G. Physical Principles of Nanoparticle Cellular Endocytosis. *ACS Nano* **2015**, *9*, 8655–8671. [CrossRef] [PubMed]
69. De Jong, W.H.; Hagens, W.I.; Krystek, P.; Burger, M.C.; Sips, A.J.; Geertsma, R.E. Particle size-dependent organ distribution of gold nanoparticles after intravenous administration. *Biomaterials* **2008**, *29*, 1912–1919. [CrossRef] [PubMed]
70. Kang, Y.; Xu, L.; Dong, J.; Yuan, X.; Ye, J.; Fan, Y.; Liu, B.; Xie, J.; Ji, X. Programmed microalgae-gel promotes chronic wound healing in diabetes. *Nat. Commun.* **2024**, *15*, 1042. [CrossRef]
71. Zhang, F.; Kang, Y.; Feng, L.; Xi, G.; Chen, W.; Kong, N.; Tao, W.; Luan, T.; Koo, S.; Ji, X. Infected wound repair with an ultrasound-enhanced nanozyme hydrogel scaffold. *Mater. Horiz.* **2023**, *10*, 5474–5483. [CrossRef]
72. Singh, K.; Yadav, V.B.; Yadav, U.; Nath, G.; Srivastava, A.; Zamboni, P.; Kerkar, P.; Saxena, P.S.; Singh, A.V. Evaluation of biogenic nanosilver-acticoat for wound healing: A tri-modal in silico, in vitro and in vivo study. *Colloids Surf. A Physicochem. Eng. Asp.* **2023**, *670*, 131575. [CrossRef]

Disclaimer/Publisher's Note: The statements, opinions and data contained in all publications are solely those of the individual author(s) and contributor(s) and not of MDPI and/or the editor(s). MDPI and/or the editor(s) disclaim responsibility for any injury to people or property resulting from any ideas, methods, instructions or products referred to in the content.